Desalination and Water Treatment
www.deswater.com
doi: 10.5004/dwt.2020.26182

202 (2020) 133–149
October

Simulation and optimization of hydraulic conditions via separation mesh modification in a pilot hybrid growth membrane bioreactor using computational fluid dynamics

Ahmed Bakr[a,b,c], Bo-Wen Wang[c], He-Ping Liu[d], Xue-Song Yi[a,b,c], Fei Yang[a,b,c,*]

[a]*Center for Eco-Environmental Restoration Engineering of Hainan Province, Renmin Avenue 58, 570228 Haikou, China, Tel. +86-898 6629 1290; Fax: +86-8986619 2915; emails: fei.yang@hainanu.edu.cn (F. Yang), ab.eeaa@yahoo.com (A. Bakr), cedar401@163.com (X.-S. Yi)*
[b]*Key Laboratory of Agro-Forestry Environmental Processes and Ecological Regulation of Hainan Province, Renmin Avenue 58, 570228 Haikou, China*
[c]*Department of Environmental Science and Engineering, Hainan University, Renmin Avenue 58, 570228 Haikou, China, email: 2453125215@qq.com (B.-W. Wang)*
[d]*Central Iron and Steel Research Institute, Xueyuan South Road 76, Haidian District, 100081 Beijing, China, email: liuhp07@163.com (H.-P. Liu)*

Received 26 January 2020; Accepted 1 June 2020

ABSTRACT

The hydraulic conditions play an essential role in enhancing membrane fouling control and reducing energy consumption in hybrid growth membrane bioreactors (HG-MBRs). In the current research, to optimize the hydraulic conditions of a pilot HG-MBR, the effects of modifying the separation mesh between the membrane area and the carrier area were systematically investigated by placing baffles of different sizes at different locations. A computational fluid dynamics Eulerian–Eulerian two-dimensional simulation model was also established to describe the effect of the aeration rates on the carriers' mobility in the reactor. The simulation results were successfully validated against the experimental results with a good agreement. The validated simulation results revealed that using a baffle could enhance the hydrodynamic characteristics of the reactor, relieve the negative impact of the separation mesh on the carrier mobility, and reduce the aeration intensity required to drive the recirculation of the carrier in the reactor, therefore reducing the energy consumption. Under the optimal operation conditions, a baffle with an area of 0.71 m^2 (0.84 m × 0.84 m) and located on the upper part of the mesh allowed the aeration to be decreased by more than 15% at a filling ratio of 50%, which would represent significant energy savings in the reactor design.

Keywords: Computational fluid dynamics simulation; Energy saving; Hybrid growth membrane bioreactor; Hydraulic condition; Separation mesh

1. Introduction

Hybrid growth membrane bioreactors (HG-MBRs) is a novel biological reactor combined membrane separation process with a hybrid growth process, in which both activated sludge and attached biofilm processes are cooperative for wastewater treatment efficiently [1]. The use of advanced HG-MBRs has been acknowledged as a promising technique to increase wastewater treatment efficiency [1–4]. The membrane unit can be either submerged [5] or externally configured to an HG-MBR [2,6]. However, by reason of the complex multiphase flow and biological processes in HG-MBRs, their operation mechanisms, including their hydrodynamic characteristics, have not yet been adequately studied. Therefore, dedicated experiments are needed to entirely understand their hydrodynamic processes.

* Corresponding author.

The separation mesh plays a serious role in HG-MBRs [7]. The mesh divides the reactor into a carrier area and a membrane area to protect the membranes from being damaged by the carriers. It is conceivable that the geometric configuration, such as the area of the closed region of the mesh, could have actual impacts on the hydraulic conditions of an HG-MBR. Therefore, optimization of the separation mesh configuration deserves careful consideration [8].

Despite the significance of the separation mesh, little information regarding the optimal design of HG-MBRs is available, and an understanding of the detailed effects of the mesh configuration on the hydraulic circumstances in the membrane tank is lacking [8]. Few experimental studies on this theme have been carried out, possibly due to the difficulty of measuring the hydrodynamics due to the intrusive impacts of measurement on the test flow [9]. In this context, mathematical modeling studies have been carried out more often, and several simplified empirical models have been proposed to predict some collective hydrodynamic properties, such as the average cross-flow velocity in the riser section [10]. Even so, most of these models cannot provide adequate quantitative information (e.g., spatial distributions of the gas hold-up, water velocity, and membrane surface shear) for an elaborate mesh design [8].

Researchers have dedicated great effort to decrease the power demand of MBR plants. Some research in this area has focused on optimization of the operating conditions, such as the cyclic aeration systems [11–13]. The airlift configuration, in which membranes are sandwiched between baffles, can obviously improve the cross-flow along the membrane surface [10], and both the baffle size and location have been proven to have an important impact on improving the hydrodynamic characteristics of MBRs [8]. However, MBR optimization has mostly continued in the experimental stage. It can be promoted from the experimental stage to the computer simulation stage via the evolution of computer science [14]; computational fluid dynamics (CFD) have been advanced to simulate accurately [15] and reflect the characteristics of the flow field in HG-MBRs [16–18].

Hydrodynamic CFD models are effective tools for the design and optimization in which virtual prototyping has a much lower expenditure comparing with conducting pilot-scale experiments [19–20]. But for a long time, the three-dimensional numerical simulation was limited by computer power and run-time therefore the two-dimensional (2D) models were the preferred ones for the analysis of the flow structure. A lot of interesting results were obtained using the two-dimensional approach and a set of bright ideas was based on these numerical simulations. The known restrictions of the 2D approach cause the question of the validity of used models and of reliability of obtained results. This means that the 2D models give a rather adequate results in the numerical simulation of the flow processes prediction with a reduction of the run time.

However, few 2D CFD simulations have been carried out in interconnected fluidized beds due to their complex geometry and flow physics, which demand high computational resources [21–24]. Although major promotion has been made recently, a significant development in the use of the CFD technique is still required.

Therefore, the current research aims to use CFD simulation for investigating the effect of the aeration rates on the recirculation of the carriers in the HG-MBR and to find an optimized separation mesh configuration incorporating a baffle to enhance the aeration efficiency. The influences of the area and location of the baffle on the hydrodynamic characteristics and fluidity in the HG-MBR are clarified, and the structure of the reactor is optimized for energy-saving operation. The obtained CFD simulation results were validated against the real experiments in a pilot HG-MBR.

2. Materials and methods

2.1. Experimental setup

The pilot HG-MBR was set up as shown in Fig. 1. The apparatus consisted of an aerobic reactor tank equipped with a submerged ultrafiltration flat-sheet membrane module (Microdyn-Nadir Xiamen Co. Ltd.). The membrane was made from polyethersulfone with an effective surface area of 10 m^2, a nominal membrane pore size of 0.04 μm (150 kDa). The aerobic reactor tank was made of 304 stainless steel and had a size of 0.98 m × 0.84 m × 1.96 m (length × width × height), a working volume of 1.48 m^3 with an effective water depth of 1.8 m, and an intermediate separation mesh (perforated stainless steel plate, pore diameter: 8 mm). The separation mesh divided the reactor into two zones: a carrier zone containing carriers for hybrid growth with a volume of 0.98 m^3, and a membrane zone containing the membrane module with a volume of 0.5 m^3. The baffles used in the experiment consisted of several stainless-steel sheets of the following sizes: I. 0.35 m^2 (0.42 m × 0.84 m); II. 0.71 m^2 (0.84 m × 0.84 m); III. 1.06 m^2 (1.26 m × 0.84 m) that could be fixed to adjust the covered area to represent 25%, 50%, and 75% of the area of the separation mesh. The baffle locations were also set to upper, middle and lower as needed to adjust the closed area of the separation mesh partially which effect on the interference of the rising airflow comes from the air tubes at the bottom of the reactor and enters the carriers' zone and membrane zone through the mesh. Thus optimize the hydraulic characteristics in the reactor.

Three microporous aeration tubes designated as A, B, and C were installed at the bottom of the carriers' zone (B and C) and membrane zone (A), respectively (Fig. 1); tubes B and C drove the circulating flow of the carriers while supplying oxygen, and tube A flushed the membrane surface to mitigating membrane fouling. The parameters of the carriers used are shown in Table 1.

2.2. Experimental operation conditions

The experiments were carried out with tap water in the wastewater treatment plant of Haikou City, Hainan province, P.R. China. Most of the experiments were operated without membrane filtration, except the water inlet/outlet flow experiment when the membrane was run with a filtration flux of 20 LMH at 5 min filtration/30 s relaxation mode.

During experimental operation, different baffle locations (upper, middle, and lower) and size configurations were applied to determine the effects of the baffle configurations on the hydrodynamics in the reactor.

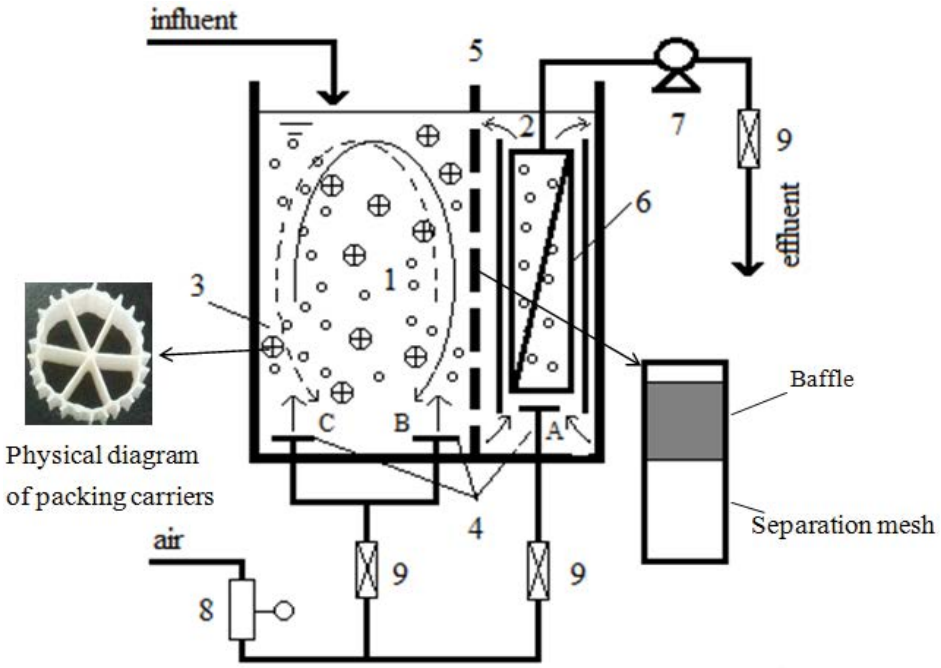

Fig. 1. Schematic diagram of the HG-MBR. (1) Carriers' zone; (2) membrane zone; (3) packing carriers; (4) aeration tubes (A, B, C); (5) separation mesh; (6) membrane module; (7) suction pump; (8) gas roots flow meter; (9) air/water flow meters. *Note*: Fig. 1 shows a schematic diagram of the baffle on the separation mesh (circular punch on the separation mesh is not shown).

Table 1
Parameters of the carriers used

Parameter	Description
Material	Polyethylene
Size (mm)	Φ15 × 11 (high)
Density (g cm^{-3})	About 0.96
Specific surface area (m^2 m^{-3})	About 600
Filling ratio	20% and 50%

The demanded aeration rates for the fluidizations of the used carriers filling rates in a pilot HG-MBR. The aeration volume was adjusted by the intake valve, and the fluidization state of the carriers in the carriers' zone was characterized by the area of the flowing carriers as a percentage of the area of the water surface in the carriers' zone. The corresponding intensity of aeration needed to achieve a given fluidization state was recorded. The carrier filling ratio is the ratio of the packing volume of the carriers to the effective volume of the carrier zone. The experiment was carried out using two typical filling ratios of 20% and 50%.

The three aeration tubes (A, B, and C tubes) were combined in the following four ways: (1) B-tube single-side aeration; (2) C-tube single-side aeration; (3) A + B tube combined aeration; (4) A + C tube combined aeration. Based on the membrane module parameters and membrane pollution control needs, the aeration rate of the A-tube was set to 5 m^3/h.

The specific experimental conditions are scheduled in Table 2, and a schematic diagram of the area and location of the baffles is shown in Fig. 2.

2.3. CFD modeling simulation

In the present work, an Euler–Euler two-fluid model was employed to investigate the flow field of the HG-MBR. The basic idea of the CFD method is to represent the fields of the physical quantities, which have been continuously distributed in time and space, using a series of finite values of discrete points. The principle and method are used to establish the algebraic equations that describe the relationships between the field variables at these discrete points and then numerically solve the algebraic equations to obtain the internal hydraulic characteristics. Through this numerical simulation method, the basic physical quantities (such as the distribution of volume fraction and so on) of various spatial sites within the flow field with extremely complicated problems can be obtained. In addition, compared with the experimental method, the CFD method can significantly reduce the number of experimental tests, save a lot of money and time, and can solve some problems that are difficult to measure because of the experimental technique [25].

2.3.1. Domain geometry, mesh, and boundary conditions

The geometry and meshes were established using the design modeler and meshing features of the software ICEM. The geometry of the domain and membrane bundle was simulated as a wall. The domain geometry was simplified to a 2D representation, it is shown in Fig. 2.

A structured hexahedral mesh was employed for its superior mesh quality and calculation convergence control. The computational results were obtained to be autonomous

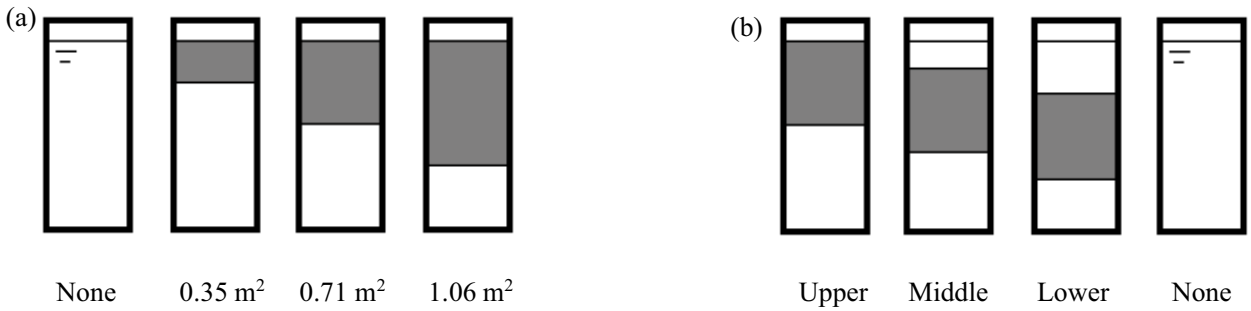

Fig. 2. Schematic diagram of the (a) baffle areas and (b) locations at which the baffle was attached to the separation mesh. *Note*: circular perforations in the mesh are not shown.

of the elements number of 101,000 elements. The boundary condition set in the three aeration tubes is velocity inlets (velocity-inlet) using FLUENT, and the constant-velocity magnitude is 0.083 m/s; the water level was set as the degassing condition. The grid refinement of the air inlet and some phase interfaces are to obtain higher accuracy. Therefore, the air only was allowed to flow out of this boundary, while all the other boundaries were adjusted as no-slip walls.

The top boundary condition is the gas outlet (degassing). The internal boundary of the calculation domain is set to be mostly interior, which does not affect the movement of the material. The remaining boundary conditions are walls, which limits the material in the calculation domain without causing material loss.

Three zones are preset to facilitate subsequent setup in the solver. In the initial state, the simulation time is 0s; the purple area is the pure water area; the green area is the area where the carriers were mixed with water when the carriers' filling ratios are 20% and 50%; the red area is the pure air area. Each phase of the simulation process is an incompressible phase, and the liquid level will definitely rise during the aeration process. In order to prevent errors caused by material overflow, a pure air area was set.

2.3.2. Governing equations

In the Eulerian–Eulerian multiphase model, the volume fractions represent the ratio of the volume employed by each phase (water, carriers, and air); over the computational cell

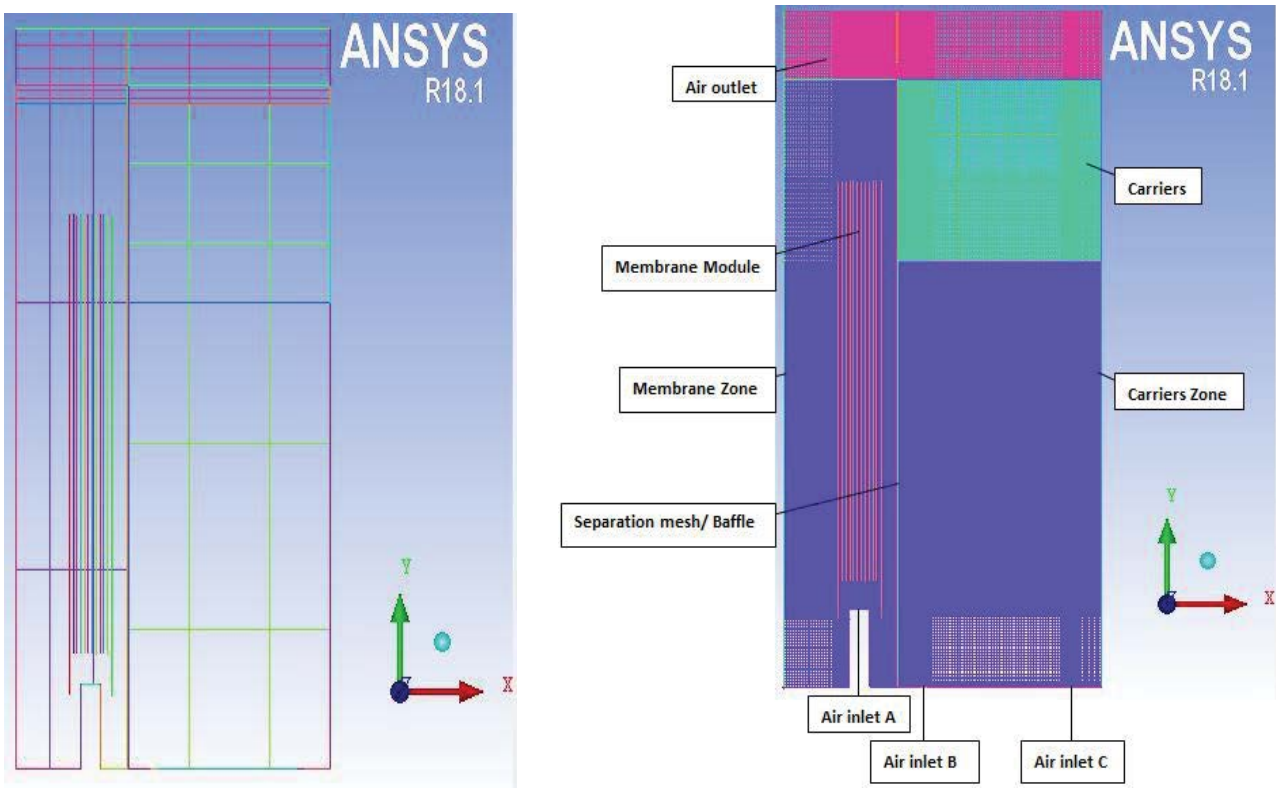

Fig. 3. 2D geometry of the computational domain and the mesh of the pilot HG-MBR.

Table 2
Experimental conditions used to test the effect of the area and location of the baffle on the hydrodynamic characteristics

S. No.	Experimental setup	Baffle area (m^2)	Baffle location	Aeration method	Carrier filling ratio	Water flow mode
1	Influence of the baffle area	0.35 0.71 1.06 No baffle (for comparison)	Upper	C-tube A + C tube	20%, 50%	Static
2	Influence of the baffle location	0.71	Upper Middle Lower part No baffle (for comparison)	B-tube C-tube A + B tube A + C tube	50%	Static
3	Combined influence of the baffle area and location	0.35 0.71 1.06	Upper Middle Lower part	C-tube A + C tube	50%	Static
4	Influence of inlet and outlet modes and aeration rate of membrane zone	0.71	Upper	A + C tube	50%	Static, dynamic

Notes:
- Area and size of the baffles: I. 0.35 m^2 (0.42 m × 0.84 m); II. 0.71 m^2 (0.84 m × 0.84 m); III. 1.06 m^2 (1.26 m × 0.84 m).
- Location and distance of the upper end of the baffle on the mesh affined to the water surface: I. upper location (0 m from the water surface); II. middle location (0.25 m from the water surface); III. lower location (upper end 0.5 m from the water surface).
- Static water flow mode: no inflow or outflow. *Dynamic mode*: inlet and outlet flow of about 200 L/h.
- During the investigation of the influence of the aeration intensity in the membrane zone, the A-tube aeration intensity was set to 4, 5, or 6 m^3/h. During all other experiments, it was set to 5 m^3/h.

volume; the conservation laws of the continuity, momentum, and turbulent equations are solved for each phase, while all the phases shared a single pressure. The general governing equations considered for unsteady and multiphase flow are listed as follows:

2.3.2.1. Continuity equations

The continuity equation [26] for phase q is:

$$\frac{\partial}{\partial t}\left(\alpha_q \rho_q\right)+\nabla\cdot\left(\alpha_q \rho_q \vec{v}_q\right)=\sum_{\rho=1}^{n}\left(\dot{m}_{pq}-\dot{m}_{qp}\right)+S_q \tag{1}$$

where α_q, ρ_q and $\vec{v}_q$ are the density and velocity of phase q, respectively. m_{pq} represents the mass transfer from the p^{th} to q^{th} phase; m_{qp} symbolizes the mass transfer from phase q to phase p. The last term S_q is the source.

2.3.2.2. Momentum equations

The momentum equation [27] for phase q is:

$$\frac{\partial}{\partial t}\left(\alpha_q \rho_q \vec{v}_q\right)+\nabla\cdot\left(\alpha_q \rho_q \vec{v}_q \vec{v}_q\right)=-\alpha_q \nabla p+\nabla\cdot\bar{\bar{t}}_q+\alpha_q \rho_q \vec{g}+\sum_{\rho=1}^{n}\left(\vec{R}_{pq}+\dot{m}_{pq}\vec{v}_{pq}-\dot{m}_{qp}\vec{v}_{qp}\right)+\left(\vec{F}_q+\vec{F}_{\text{lift},q}+\vec{F}_{wl,q}+\vec{F}_{vm,q}+\vec{F}_{td,q}\right) \tag{2}$$

where $\bar{\bar{\tau}}_q$ is the q^{th} phase stress–strain tensor [28].

$$\bar{\bar{\tau}}_q=\alpha_q\left(\nabla\vec{v}_q+\nabla\vec{v}_q^{T}\right)+\alpha_q\left(\lambda_q-\frac{2}{3}\mu_q\right)\nabla\cdot\vec{v}_a\bar{\bar{I}} \tag{3}$$

where μ_q and λ_q are the shear and the bulk viscosities of phase q, respectively; $\vec{F}_q$ is an external body force; $\vec{F}_{\text{lift},q}$ is a lift force; $\vec{F}_{Wl,q}$ is a virtual mass force; $\vec{F}_{td,q}$ is an interactive force between phases; p is the pressure shared by all the phases; $\vec{v}_{pq}$ is the interphase velocity.

2.3.2.3. Flow equations

CFD simulation of systems involving fluid flow has a significant role in the understanding and visualization of the dynamics of these complex systems as well as in the prediction of the flow behavior and associated phenomena of such systems. The flow equations were described as follows (4).

$$\frac{\partial}{\partial t}\left(\alpha_k \rho_k \varphi_k\right)+\nabla\cdot\left(\alpha_k \rho_k u_k \varphi_k\right)=\nabla\cdot\left[\alpha_k \Gamma_k^{\varphi}\left(\nabla\varphi_k\right)\right]+S_k^{\varphi} \tag{4}$$

where t is the time (s); α_k is the volume fraction of phase k (dimensionless); ρ_k is the density of phase k (kg/m^3); ϕ_k is the arbitrary physical quantity of phase k; u_k is the velocity of phase k; Γ_k^{ϕ} is the physical quantity of phase k with a diffusion coefficient of ϕ; S_k^{ϕ} is the source of the k physical quantity ϕ.

2.3.2.4. Turbulence model equations

The turbulence model is based on the Reynolds-averaged kinetic equation and the pulsation equation. In the multi-phase model, there are three different methods to simulate multiphase turbulence, which are mixed turbulence model, dispersed turbulence model, and turbulent turbulence model. The mixture turbulence model is mainly suitable for multi-phase flow of phase separation or stratification with a phase density ratio close to 1. The model considers the turbulent flow of the continuous phase and dispersed phase as the turbulent flow of the mixture, and does not solve for the turbulence of the individual phases particularly. However, the k–ε model is the most common turbulence model. The k–ε turbulence model can be divided into three types: standard k–ε model (renormalization group k–ε model, RNG k–ε model), and realizable k–ε model [29]. Both the realizable k–ε model and the RNG k–ε model show better performance than the standard k–ε model in strong streamline bending, vortices, and rotations. The studies have shown that the realizable k–ε model works well for flow separation and complex secondary flows in all k–ε models [30]. The studies also revealed that among the available k–ε models, the realizable k–ε model has a good effect on flow separation and complex secondary flow [31]. The equations for k and ε are described as follows:

$$\frac{\partial}{\partial t}\left(\rho k\right)+\frac{\partial}{\partial x_j}\left(\rho k u_j\right)=\frac{\partial}{\partial x_j}\left[\left(\mu+\frac{\mu_t}{\sigma_k}\right)\frac{\partial k}{\partial x_j}\right]+G_k+G_b-\rho\varepsilon-Y_M+S_k \tag{5}$$

$$\frac{\partial}{\partial t}\left(\rho\varepsilon\right)+\frac{\partial}{\partial x_j}\left(\rho\varepsilon u_j\right)=\frac{\partial}{\partial x_j}\left[\left(\mu+\frac{\mu_t}{\sigma_\varepsilon}\right)\frac{\partial\varepsilon}{\partial x_j}\right]+\rho C_1 S_\varepsilon-\rho C_2\frac{\varepsilon^2}{k+\sqrt{v\varepsilon}}+C_{1\varepsilon}\frac{\varepsilon}{k}C_{3\varepsilon}G_b+S_\varepsilon \tag{6}$$

where ρ and u_j are the density and velocity, respectively; μ_t is the turbulent viscosity; G_k is defined as the generation of turbulent kinetic energy due to the mean velocity gradients; G_b is defined as the generation of turbulent flow energy caused by buoyancy; The turbulent Prandtl numbers for k and ε are σ_k = 1.0 and σ_ε = 1.3, where k is the turbulent kinetic energy k = 0.8, ε is the energy dissipating rate of turbulent kinetic energy ε = 0.9; S_k and S_ε are defined sources. The coefficients constants involved in Eqs. (5) and (6) are C_μ = 0.09, C_1 = 1.44 and C_2 = 1.92 respectively.

2.3.3. Numerical analysis and considerations

The numerical simulations were obtained using a convergence criterion of 10^{-5} for each scaled residual component and a time step of 5×10^{-4} s. As the mesh quality has a direct influence on the simulation convergence, computational time and simulation accuracy. So, different mesh elements were tested to select a suitable mesh that produces accurate results and reasonably fast simulation. The geometry was meshed into 92,792 elements, 101,000 elements and 126,680 elements. The air velocity results from

the simulation results were compared with the experimental results to choose the appropriate simulation mesh. The simulation results with the mesh 101,000 elements shown a relatively good agreement with the experimental results. Therefore, the computational domain of the reactor was discretized into 101,000 quadrilateral cells. This mesh is considerably larger than the particle size and is smaller than the system dimensions which satisfies the mesh criterion in the numerical method for smooth convergence. This grid independence test performed in the current research also led to observations comparable to those of the reports of many investigators that if the numerical cell size is about 10 times of the particle size, it can capture the hydrodynamics in fluidized bed reactors obviously [32].

The boundary conditions were fixed by specifying the inlet velocity and outlet pressure values at the reactor inlet and outlet, respectively. Some of the key parameters used in the simulation are presented in Table 3.

2.4. Experimental validation

The model was based on a pilot HG-MBR plant. The first step of the CFD simulation was validation of the influence of the baffle area and location on the hydrodynamic characteristics, which was conducted by considering the airflow and carrier circulation states. The validation was based on the trends observed experimentally in the HG-MBR. Simulated cases were progressed under steady-state conditions. These conditions were utilized to analyze the flow and species distribution while maintaining the continuous and stable operation of the reactor. The airflow was measured along certain lines in the reactor and compared with the airflow profiles at the same locations in the CFD simulation to validate the CFD results. The fluid region should have the same geometry as the real reactor, and the operation conditions should also be the same.

Due to the difficulties to describe the hydrodynamic characteristics and the aeration flow ratios required to the recirculation of the carriers, the aeration flow ratios in the reactor were computed using the CFD simulation model for a clear investigating and optimizing then validated against the experimental results.

Therefore, the air-flow rate Q is given by:

$$Q\ (\mathrm{m^3/S}) = A \cdot V \tag{7}$$

where V (m/s) is the average air velocity at the designated point and A (m^2) describes the air channel area at a designated point. A can be deduced from the construction plans so the computation of Q is based on A and V, which are obtained from simulation data.

Table 3
Physical performance parameters of the simulated HG-MBR

Parameter	Air	Carrier	Water
Density ρ (kg/m^3)	1.225	998.2	998.2
Viscosity μ (kg/m-s)	1.7894e-05	–	0.001003
Temperature T (k)	300	300	300

3. Results and discussion

A multiphase CFD Eulerian–Eulerian two-dimensional model was numerically simulated to describe the hydrodynamics of the fluid flows in the reactor. The carrier particles were preferred to be smooth, cylindrical, and inelastic and to undergo binary collisions. An initial driving force (i.e., the intensity of aeration when the carriers begin to flow) was required to initiate flow from the stationary state, and the magnitude of the initial driving force was correlated to the filling ratio and aeration method.

The way in which the fluidization state of carriers has been described has varied among researchers; fluidization has been qualified using concepts such as homogeneous fluidization, inhomogeneous fluidization, and other methods [33], or classifying the observed intensity of the "activity" of the carrier in water as one of five levels: silt, weak, ordinary, complete, and fierce. These description methods are difficult to quantify and apply during experiments. In the present simulation, the percentage area of the flowing carriers relative to the total area of the water surface in the carriers' zone was used to clarify the fluidization state of the carriers. A numerical tool to simulate the flow characteristics in the HG-MBR was developed.

As the aeration intensity is gradually increased, the carriers tend to enter the flow. The state at which the flowing carrier area was about 50% of the water surface was defined as the starting flow state, and the aeration intensity at this state was defined as the initial flow driving force. When the flowing carrier area reaches about 95%, only a small amount of carrier residue remains in the turbulent dead zone, and sinking occurs within 5 s. This state was defined as the full flow state, and the corresponding aeration intensity was denoted as the full flow driving force. The intermediate fluidization states can be collectively referred to the general flow state. This study focused on the initial flow and full flow states of the carriers. The average airflows in the simulated and experimental results in these states were compared. The simulation results were found to be correlated with the experimental data, which verified the airflow in the simulation.

For experimental validation, different baffle location scenarios were applied, namely, the upper, middle, and lower location scenarios. The baffle size was varied in each scenario to find out the effect of the baffle size on the hydrodynamics in the reactor. The optimized conditions were then compared with the baffle-free conditions to evaluate the effectiveness of the baffle in reducing aeration demand. The results were then used to validate the CFD simulation. In addition, the capability of CFD to display results effectively is an invaluable tool. Therefore, the comparison between the experiment and simulation provided interesting information.

3.1. Influence of the baffle area on the hydrodynamic characteristics

The C-tube and combined A + C tube aeration methods were used to compare the effects of different baffle

areas on the hydrodynamic characteristics at two carrier filling ratios (20% and 50%). The results from the simulation and the experiments are shown in Figs. 4 and 5. The simulation results were in excellent agreement with the experimental trends, indicating the reliability of the situation and thus allowing us to move on to the next simulation scenarios. At both filling ratios, the aeration rates (i.e., the energy consumption) required to start the initial flow and full flow of the carriers decreased with increasing baffle area, although only a small change was observed for the starting flow at a 20% filling ratio. This indicated that the separation mesh had a negative dissipation effect on the flow driving the carriers. The use of a baffle could significantly improve the hydrodynamic characteristics of the reactor and promote the circulation of the carriers, thus reducing energy consumption, especially at high carrier filling ratios (such as 50%). In an experimental comparison with the baffle-free system, the use of a baffle with an area of 0.71 m^2 (0.84 m × 0.84 m) reduced the aeration rate required for complete carrier fluidization by 54.2% when only the C-tube was used for aeration, and by 15% when both the A + C tubes were used as shown in Table 4. This reduction was as a result of the blocking and guiding effect of the baffle on the flow of the circulating water, and the changes to the hydrodynamic characteristics of the carrier area induced by the baffle; the driving force generated by the C-tube was concentrated downward on the baffle side. The energy consumption was also reduced due to the reduction of required aeration at these optimal conditions in the reactor. The experimental heterogeneity of the circulation of the air and carriers was well predicted by the simulation model. Therefore, the negative effect of dissipation through the separation mesh to the membrane area is reduced, while the effect of the aeration driving force was increased. Fig. 6 shows the decreasing of the aeration densities under the achieved optimal hydraulic condition comparing with different operating conditions.

Obvious improvement was observed as the baffle area was increased from 0.35 to 0.71 m^2 while increasing the area further from 0.71 to 1.06 m^2 only showed a benefit for the starting flow state with the baffle in the upper location; no effect or even a negative effect was observed under other operating conditions; that is, a larger baffle area led up to increased energy consumption. This is because the upward flow caused by the membrane aeration acted as a drag force on the fluid in the channel between the two zones and increased the downward speed of the carriers, especially at the upper part of the baffle in the carrier zone.

When the baffle area is larger, the width of the bottom fluid channel between the two zones decreases, thereby reducing the drag force. When the 1.06 m^2 baffle was used, the fluid channel was almost closed, indicating the necessity of optimization. Some researchers have also verified that the drag force is more important than other types of inter-phase forces for simulating the hydrodynamics of air–carrier flow due to the great differences between the air and carrier phases. However, if the baffle area is too large, it will hinder the exchange of substances between the carrier zone and the membrane zone. This may cause the accumulation of activated sludge in the membrane zone and thereby accelerate membrane fouling. Therefore, in practical applications, the baffle area should be optimized to promote both carrier flow and substance exchange between the two regions. In addition, in the full flow state, the aeration rate required to drive the carrier flow at a 50% filling ratio was twice as high as that at a 20% filling ratio when only the C-tube was used for aeration, and 2.2 times as high when both the A + C tubes were used (excluding the A-tube aeration rate 5 m^3/h in the membrane zone). The effects of all the variables in the simulation results were also validated by the experimental results. Therefore, when determining the carrier filling ratio,

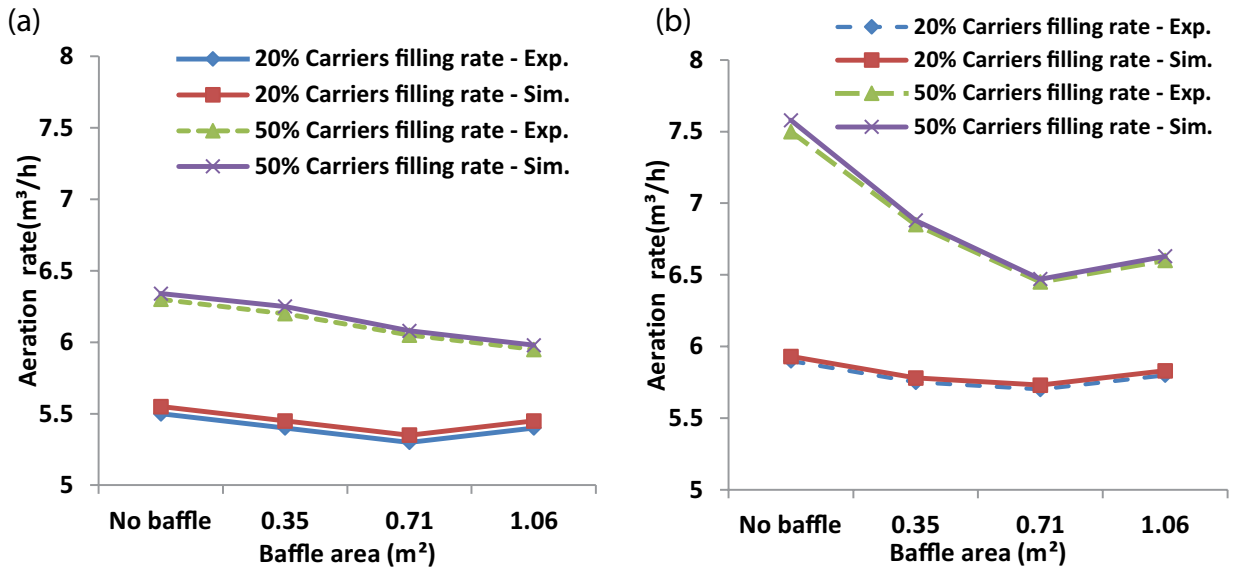

Fig. 4. Aeration flow rate required for the carriers' movements at the optimal hydraulic condition using C-tube and a combined A + C tubes for aeration and baffle areas of 0.35, 0.71, and 1.06 m^2 at the upper location part.

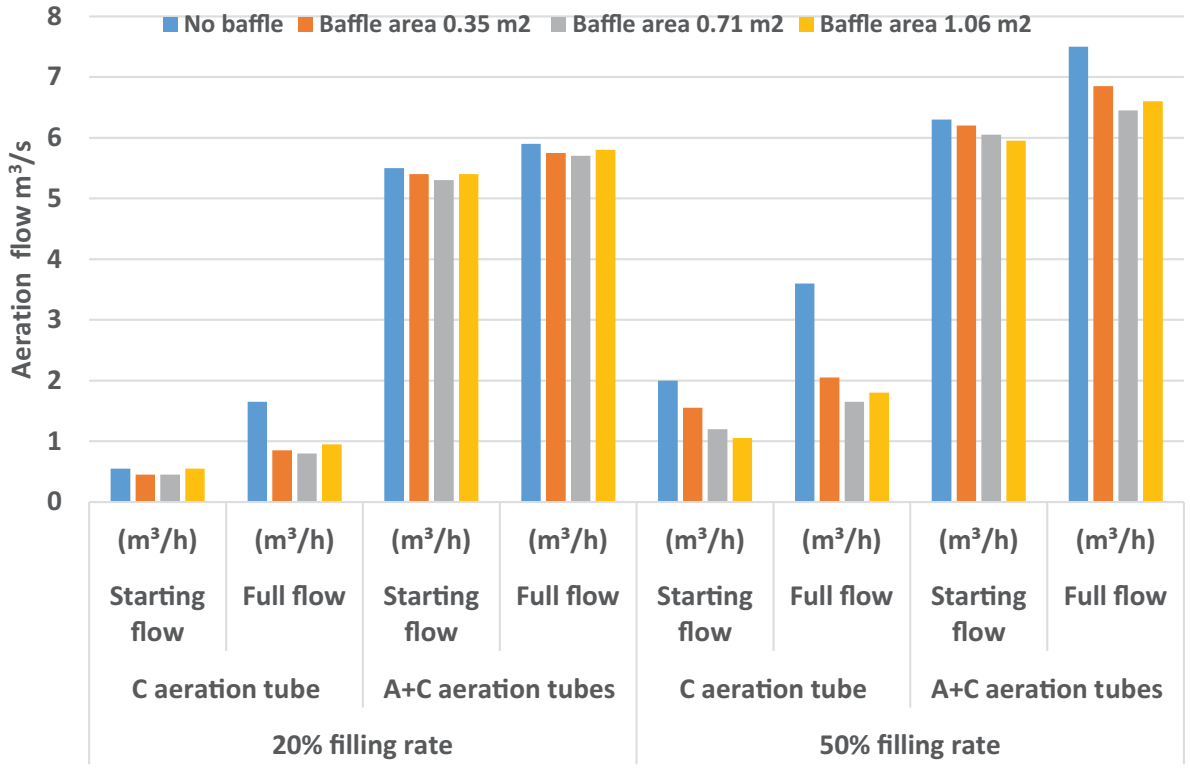

Fig. 5. Effects of the baffle area on the carrier mobility during the experiment and in the simulation using only the C-tube for aeration at 20% and 50% carrier filling ratios (a) in the starting flow state and (b) in the full flow state.

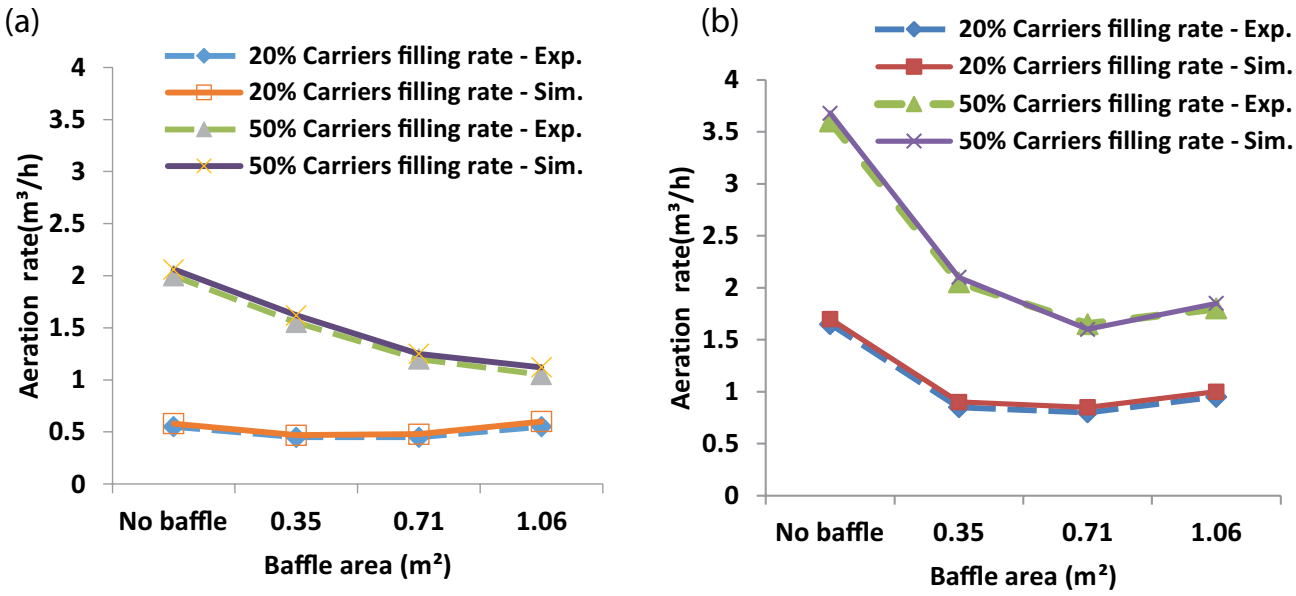

Fig. 6. Effects of the baffle area on the carrier mobility during the experiment and in the simulation using the A + C tubes for aeration at 20% and 50% carrier filling ratios (a) in the starting flow state and (b) in the full flow state.

the energy consumption needed for the driving force should be also considered. A higher carrier filling ratio results in more attached biomass, but higher energy consumption. Both these factors should be perfectly considered, along with comprehensive membrane fouling control.

Therefore, a relationship between the computed and the experimental results was built as shown in Eq. (8).

A comparison between the aeration flow ratios obtained by the CFD simulation and the aeration flow ratios obtained by the experimental measurements at the scenarios of using baffle areas 0.35, 0.71, and 1.06 m^2 on the upper location of the separation mesh and no baffle; with 20% and 50% carriers filling ratios was carried out to describe the relationship between the experimental and the computed results. The values of the air-flow ratios at these scenarios were analyzed using Statistical Package for the Social Sciences (SPSS) software and the relationship equation was formed. The comparison between the experimental and the computed results displayed a reasonable agreement. The differences for the computed and measured values of y, the predictive capability of the following equation was remarkably high (R = 0.965) as shown in the following equation:

$$y = 2.35(x_1)^{1.087}\,(x_2)^{-0.292},\ R = 0.965 \quad (8)$$

where is y is the aeration flow rate resulted from the experiment; x_1 is the carriers filling ratio; x_2 is the baffle area.

3.2. Influence of the baffle location on the hydrodynamic characteristics

The influence of the baffle location on the hydrodynamic characteristics of the reactor using different aeration methods was investigated using CFD simulation and experimental reactor operation with a fixed baffle area of 0.71 m^2 (0.84 m × 0.84 m) and carrier filling ratio of 50%; the results are shown in Figs. 7 and 8. Excellent agreement between the experiments and the simulation was again observed. In the starting flow and full flow states, the aeration rate required to drive the carrier recirculation increased as the baffle was moved downward.

Using the B-tube and the A + B tube aeration modes, the aeration rate requirements were more obvious. In the experimental results, when the B-tube aeration mode was used and the baffle was placed at the middle or lower position,

Table 4
Demanded aeration rates for the fluidizations of the used carriers filling rates in a pilot HG-MBR

Baffle area (m^2)	20% filling rate				50% filling rate			
	C aeration tube		A + C aeration tubes		C aeration tube		A + C aeration tubes	
	Starting flow (m^3/h)	Full flow (m^3/h)	Starting flow (m^3/h)	Full flow (m^3/h)	Starting flow (m^3/h)	Full flow (m^3/h)	Starting flow (m^3/h)	Full flow (m^3/h)
No baffle	0.55	1.65	5.5	5.9	2	3.6	6.3	7.5
0.35	0.45	0.85	5.4	5.75	1.55	2.05	6.2	6.85
0.71	0.45	0.8	5.3	5.7	1.2	1.65	6.05	6.45
1.06	0.55	0.95	5.4	5.8	1.05	1.8	5.95	6.6

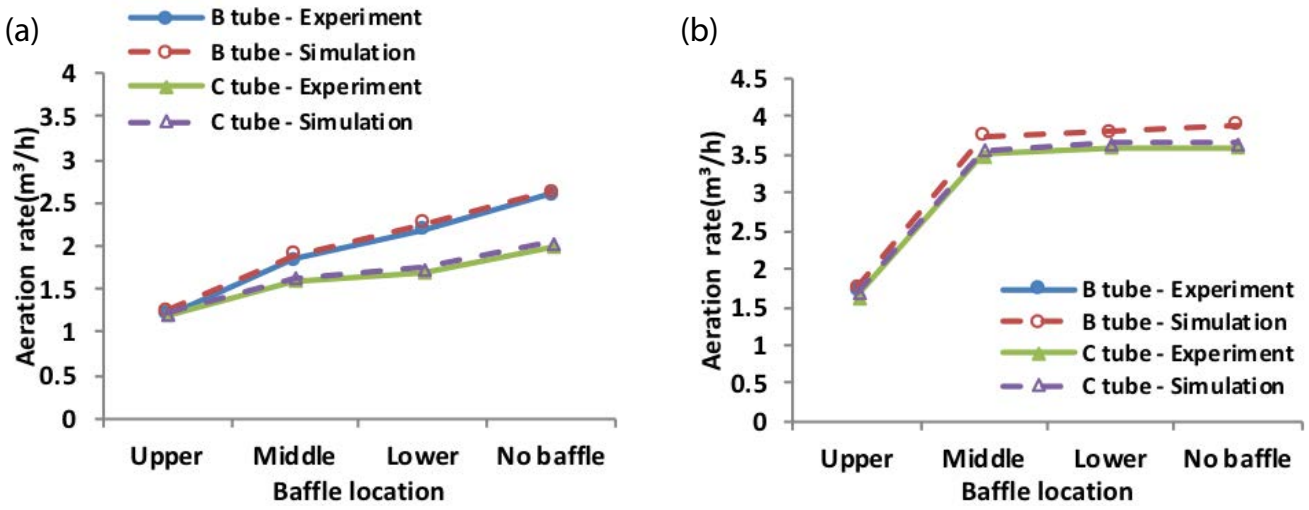

Fig. 7. Effects of baffle location on the carrier mobility in the experiment and simulation using the B-tube and C-tube aeration modes (a) in the starting flow state and (b) in the full flow state. *Note*: In (b), the dotted curve indicates that in the B-tube aeration mode, the full flow state was only reached when the baffle was in the upper position; with the baffle in the middle and lower positions, only a general-flow state was reached (approximately 80%).

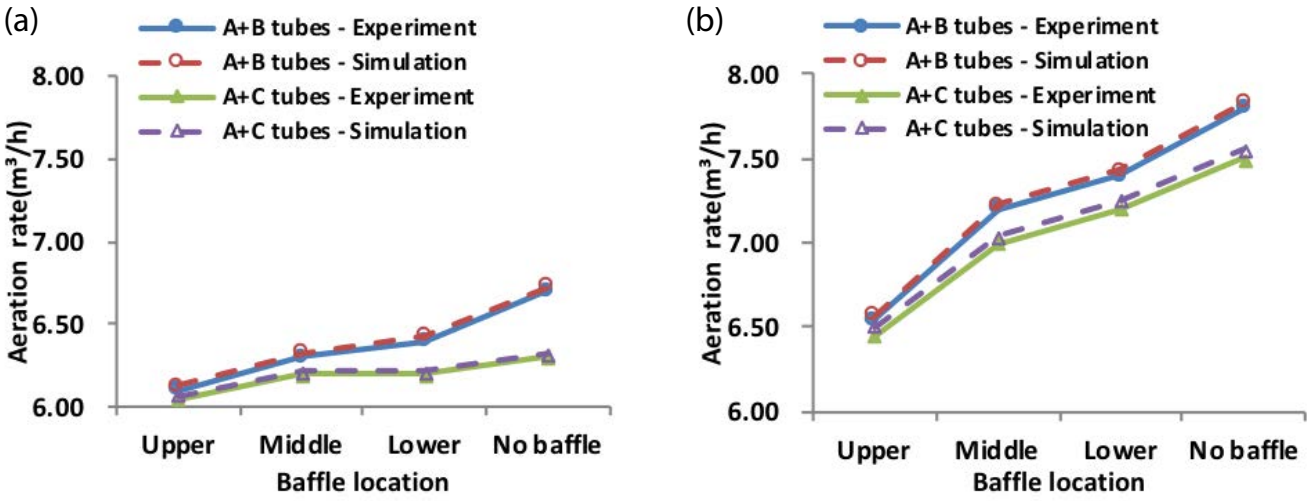

Fig. 8. Effects of the baffle location on the carrier mobility in the experiment and simulation using the combined A + B and A + C tube aeration modes (a) in the starting flow state and (b) in the full flow state.

the full flow state could not be reached, and the reactor remained in a general flow state. In the simulation results, the full flow state was achieved, but a greater air intensity was required for the upper baffle position (Fig. 7b). Using the C-tube and the A + C tube aeration modes reduced the aeration rate and energy consumption required for carrier recirculation. This confirmed the negative effects of the separation mesh on the movement of the carriers. Theoretically, the driving forces provided by B-tube and C-tube aeration should be the same. However, the B-tube is closer to the separation mesh; thus, the rising airflow from the B-tube enters the membrane zone through the mesh and loses some of its driving force, while the C-tube is nearby the reactor wall, which allows the airflow to be concentrated in the carrier zone without losing its power Fig. 9. In Fig. 10 the simulation results show that less carriers were near the separation mesh and more were accumulated at the top of the bioreactor under combined A + B aeration with no baffle on the separation mesh due to the greater aeration and liquid circulation along with the separation mesh.

The results show that the aeration rates required to drive the carrier movement were smallest when the baffle was located at the upper position for both aeration modes, indicating that this baffle position would enable energy savings. When the baffle was located at the upper position, the aeration rate needed to provide the driving force was obviously smaller, while aeration rates required with the baffle at the location of the middle or lower part were similar. From this, it could be concluded that an upper flow driving force is particularly important because in the upper part, the water flow must change direction to maintain recirculation. The water recirculation relies on not only the inertial force of the moving carriers but a continuous circulating driving force as well. The flow distribution in the tank is not uniform, especially when the C-tube aeration mode is used. The flow velocity near the upper part of the separation mesh is smaller, causing carrier retention and accumulation [34]. This phenomenon is exacerbated by the dissipative effect of the separation mesh on the driving force. The use of baffles effectively reduces this negative effect. Wu et al. [35] also used an additional wall to enhance the turbulence of the fluid in a numerical simulation of carrier recirculation in a biological contact oxidation tank.

In the combined aeration modes (Fig. 8), by deducting the A-tube aeration rate 5 m^3/h in the membrane zone from the total aeration rate, the aeration rates of the B and C tubes are smaller than the one used in the single aeration mode, accordingly. The simulation results revealed that in the A + B tube aeration mode, the carriers could reach the full flow state even when the baffle was located at the middle and lower position. This indicated that the upward flow from the membrane zone also improved the hydrodynamic characteristics of the carrier zone, and promoted carrier movement. Calculations indicated that this promotion effect was similar for both the B and C tubes. When the baffle was located in the upper position, the aeration rate could be reduced by more than 15%.

3.3. Combined influence of the baffle area and location on the hydrodynamic characteristics

To investigate the hydrodynamic characteristics of the internal flow field of the HG-MBR under different aeration rates and inlet configurations, the effects of the distribution of the airflow and flow field in the reactor under turbulent flow conditions were considered. This could provide a theoretical basis for the optimization of the membrane module, aeration intensity, and inlet locations.

The C-tube and combined A + C tube aeration modes were used, and the carrier filling ratio was 50%. Different baffle areas and locations were used for the experimental optimization; their effects on the mobility of the carriers in the experiments and simulation are shown in Figs. 11 and 12. Excellent agreement between the experiments and simulation was observed. The results show that the aeration rates required to drive the carrier movement were smallest when the baffle was located at the upper position for both aeration modes, indicating that this baffle position would enable

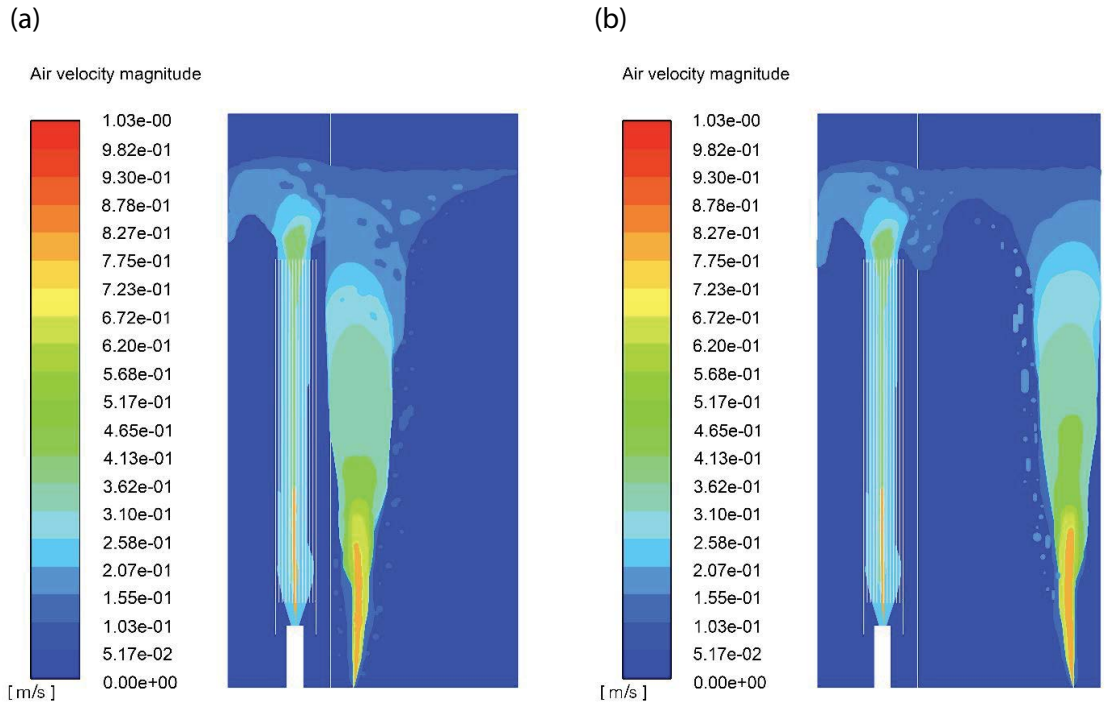

Fig. 9. Airflow velocity in the use of two situations of the operation condition (a) using a combined (A + B) aeration tubes in the starting flow state, A-tube is located in the membrane area under the membrane unit, while B-tube is located closer to the separation mesh; the rising airflow from the B-tube enters the membrane zone through the mesh, (b) using a combined (A + C) aeration tubes in the full flow state, A-tube is located in the membrane area under the membrane unit, while C-tube is located nearby the reactor wall, which allows the airflow to be concentrated in the carrier zone.

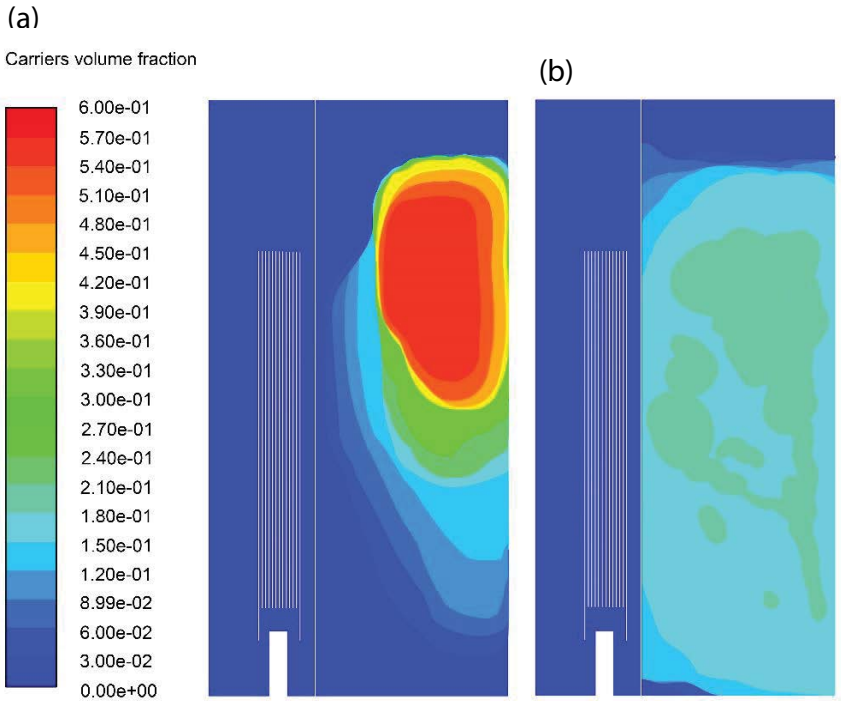

Fig. 10. Carries' volume fraction at combined A + B aeration tubes (where A aeration tube is under the membrane module and B aeration tube is close to the separation mesh) with none baffle on the air separation mesh which drove the carriers to the side of the reactor's wall and away from the separation mesh which is in a good agreement with the experimental results at the same conditions (a) in the starting flow state and (b) in the full flow state.

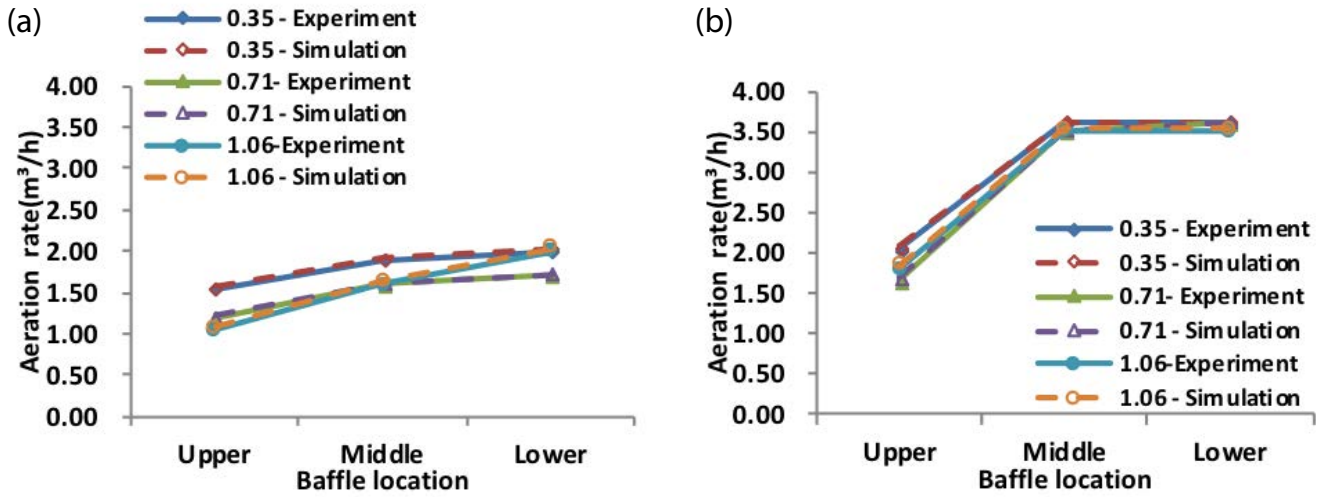

Fig. 11. Effects of the baffle area and location on the carrier mobility in the experiment and simulation using C-tube aeration and baffle areas of 0.35, 0.71, and 1.06 m^2 (a) in the starting flow state and (b) in the full flow state.

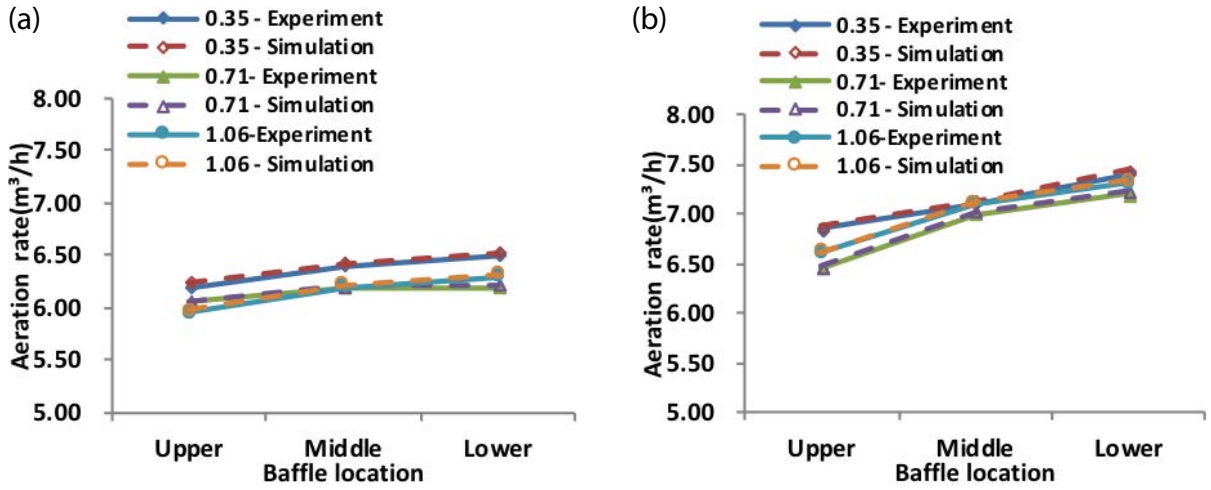

Fig. 12. Effects of the baffle area and location on the carrier mobility in the experiment and simulation using combined A + C tube aeration and baffle areas of 0.35, 0.71, and 1.06 m^2 (a) in the starting flow state and (b) in the full flow state.

energy savings. Obvious improvement was observed as the baffle area was increased from 0.35 to 0.71 m^2, while increasing the area further from 0.71 to 1.06 m^2 only showed a benefit for the starting flow state with the baffle in the upper location; no effect or even a negative effect was observed under other operating conditions; that is, a larger baffle area led up to increased energy consumption. This is because the upward flow caused by the membrane aeration acted as a drag force on the fluid in the channel between the two zones and increased the downward speed of the carriers, especially at the upper part of the baffle in the carrier zone. Fig. 13 shows the simulation results, which are opposite to those shown in Fig. 10.

When the baffle area is larger, the width of the bottom fluid channel between the two zones decreases, thereby reducing the drag force. When the 1.06 m^2 baffle was used, the fluid channel was almost closed, indicating the necessity of optimization. Some researchers have also verified that the drag force is more important than other types of interphase forces for simulating the hydrodynamics of air–carrier flow due to the great differences between the air and carrier phases [36,37]. From the above results, it was concluded that a 0.71 m^2 baffle located at the upper part of the separation mesh demonstrated optimal energy savings, and that the aeration could be reduced by more than 15% under these conditions.

3.4. Effects of the water inlet/outlet flow rates and the aeration rate in the membrane zone on the hydrodynamic characteristics

The combined A + C tube aeration mode was adopted to investigate the effects of different water inlet/outlet modes and aeration rates in the membrane zone on the hydrodynamic characteristics at a fixed carrier filling ratio of 50%.

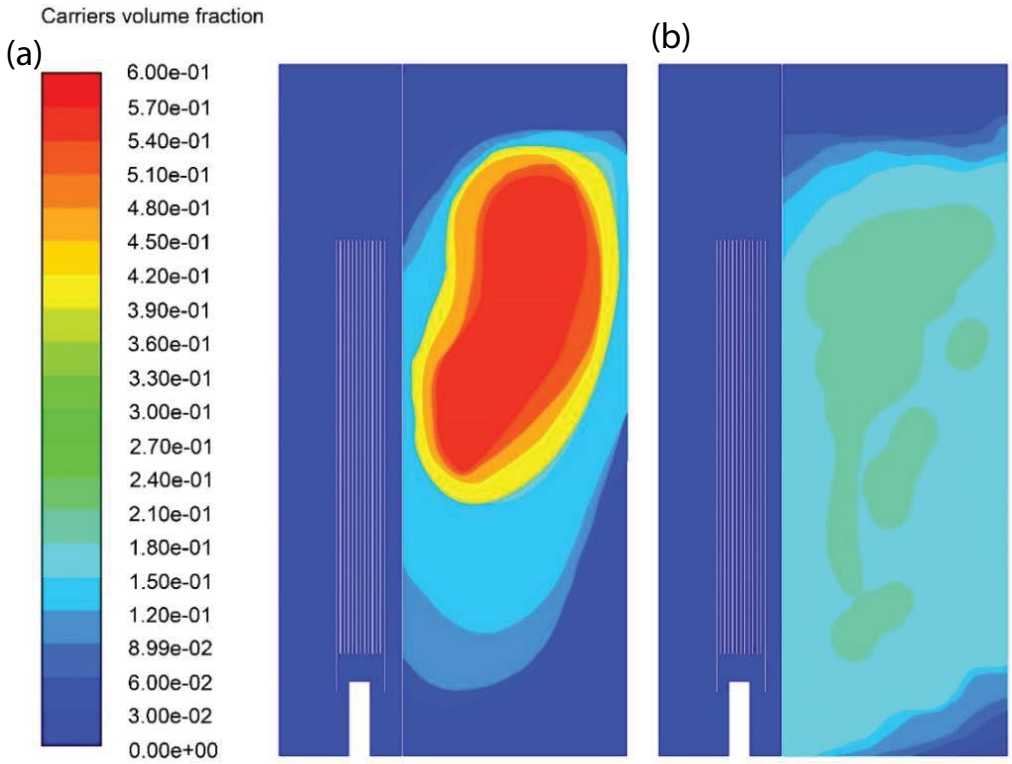

Fig. 13. Carries' volume fraction at combined A + C aeration tubes (where A aeration tube is under the membrane module and C aeration tube is close to the reactor's wall) with none baffle on the air separation mesh which drove the carriers to the side of the separation mesh and the channel between the two zones and increased the downward speed of the carriers which is in a good agreement with the experimental results at the same conditions (a) in the starting flow state and (b) in the full flow state.

The effects of the different aeration rates in the membrane zone (A-tube flow rates of 4, 5, or 6 m^3/h) on the hydrodynamic performance in the static state (no inlet/outlet water flow) and dynamic state (inlet/outlet water flow of 200 L/h) on the experimental and simulated results are shown in Fig. 14. The results revealed that excellent agreement between experiment and simulation was achieved when the carriers were in the start and full flow states. At all of the membrane zone aeration rates, little difference was observed between the aeration rate required to drive the carrier flow in the static and dynamic states, indicating that the inlet/outlet modes had almost no effect on the carrier circulation, which also confirms the previous view that the way in which water enters and leaves the reactor has little effect on the fluidization of the carriers [38]. The simulation results indicated that this low inlet/outlet water flow rate had little effect on the turbulence of the carriers and the membrane zones or on the overall flow state.

However, the aeration rates required to drive the carrier flow increased with increasing aeration rate in the membrane zone. The simulation demonstrated that greater aeration caused more flow circulation velocity and lifting force on the carriers.

When the aeration rate in the membrane zone (A-tube flow rate 4, 5, 6 m^3/h) was reduced, the C-tube aeration rate required to maintain carrier recirculation decreased slightly, indicating that the aeration intensity in the membrane zone did not significantly impact the hydrodynamic characteristics for the flushing of the membrane surface.

The factors affecting the flow recirculation in the HG-MBR for the real application can include: (1) the physical and chemical characteristics of the activated sludge, such as its particle size distribution, a viscosity [39], surface tension, etc.; (2) the operating conditions of the reactor, such as the aeration mode and intensity [40], hydraulic conditions, etc.; (3) the reactor design, such as the reactor type, configuration, and size [41] and the layout of the membrane and carrier zones, etc.; and (4) the type of carrier and filling ratio [42]. The current study shows that a simple modification to the design of the separation mesh, such as the addition of a baffle, can modify the hydrodynamic characteristics of the fluid in the reactor and effectively reduce the negative effect of the mesh on the carrier movement. Using the modified design, smooth recirculation of the carriers can be achieved using a relatively small aeration intensity, leading to energy savings.

4. Conclusions

The current study compared the results from a CFD simulation using the Eulerian–Eulerian two-phase model with the results obtained by experimental reactor operation. The CFD simulations were found to be in stellar agreement with the experimental results, indicating the accuracy,

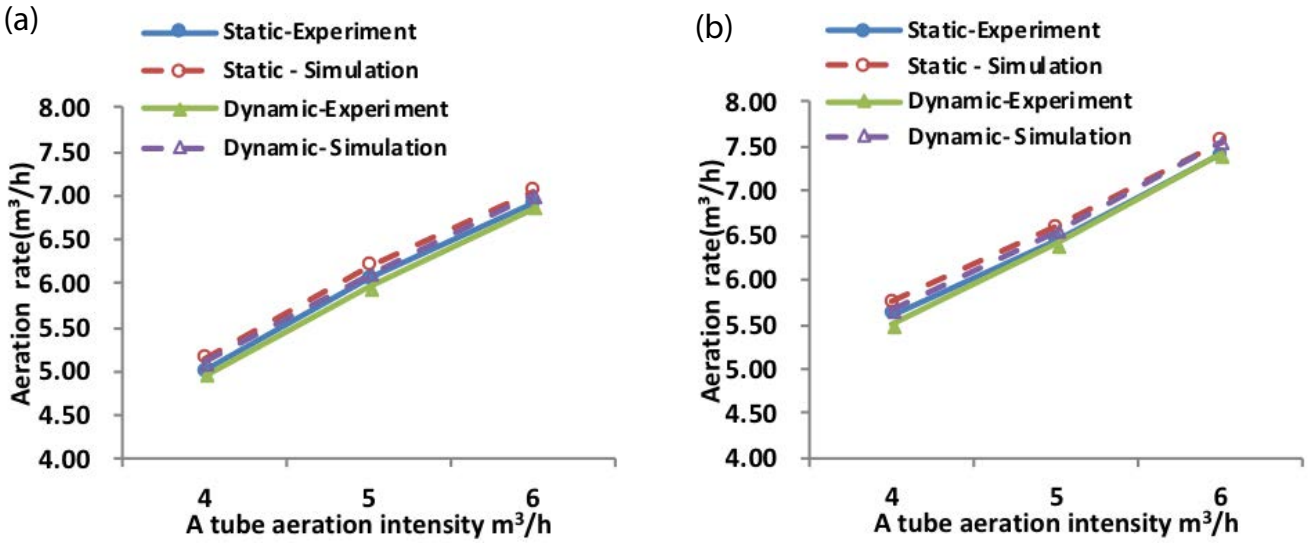

Fig. 14. Effects of the water inlet/outlet flow rates and aeration rate in the membrane zone (A-tube flow rate) on the hydrodynamic characteristics in the experiment and simulation. Baffle area: 0.71 m^2; baffle position: upper location; filling ratio: 50% (a) in the starting flow state and (b) in the full flow state.

reliability, and suitability of the CFD method for the research and prediction of bioreactor hydrodynamics. The main conclusions of the study are as follows:

- The obtained two-phase Eulerian–Eulerian simulation model could produce representative reactor conditions and flow which were very close to those of the real HG-MBR, indicating accuracy and suitability for the investigation and prediction of the hydrodynamics. The carriers tended to accumulate at the top of the bioreactor.
- The structural design of the separation mesh in an HG-MBR is an important concern to the hydrodynamic characteristics in the reactor. It could promote the recirculation of the carriers and reduce the aeration intensity, therefore reduce energy consumption. CFD models may be used as a powerful tool for the design and optimization of the separation mesh.
- In the simulation results, the optimized conditions were found to be the A + C tube aeration mode, a baffle area of 0.71 m^2 (0.84 m × 0.84 m), and the baffle position at the upper part of the mesh. Using these conditions, the aeration power required to drive the carrier movement at a filling ratio of 50% could be reduced by more than 15%.
- In the scenario of using the B-tube aeration mode with the baffle at the middle or lower position, there was a disagreement between the simulation and the experiments, where are the carriers reached the full flow state in the simulation. However, the full flow state could not be reached, and the carriers remained in a partial flow state during experiments.
- To design a filling ratio of carriers in an HG-MBR, the characteristics of the carriers, driving force, and the fluidization state should be fully taken into account. It should consider both the needs of the biological process and membrane fouling tendency.

Symbols

PES	—	Polyethersulfone
α_q and ρ_q	—	Density of phase q
$\vec{v}_q$	—	Velocity of phase q
m_{pq}	—	Mass transfer from the p^{th} to q^{th} phase
m_{qp}	—	Symbolises the mass transfer from phase q to phase p
S_q	—	Source
$\bar{\bar{\tau}}_q$	—	q^{th} phase stress–strain tensor
μ_q	—	Shear viscosity of phase q
λ_q	—	Bulk viscosities of phase q
$\vec{F}_q$	—	External body force
$\vec{F}_{\text{lift},q}$	—	Lift force
$\vec{F}_{VI,q}$	—	Virtual mass force
$\vec{F}_{td,q}$	—	Interactive force between phases
p	—	Pressure shared by all the phases
$\vec{v}_{pq}$	—	Interphase velocity
h and Q	—	Enthalpy
h	—	Thermal conductivity of the mixture
Q	—	Heat exchange between the gas phase and solid phase
Q_{pq}	—	Heat transfer when phase p changes to phase q
t	—	Time (s)
α_k	—	Volume fraction of phase k (dimensionless)
ρ_k	—	Density of phase k (kg/m^3)
ϕ_k	—	Arbitrary physical quantity of phase k
u_k	—	Velocity of phase k
Γ_k^ϕ	—	Physical quantity of phase k with a diffusion coefficient of ϕ
S_k^ϕ	—	Source of the k physical quantity ϕ

Acknowledgment

The work was supported by the National Natural Science Foundation of China (Project number: 51568018). The authors thank Beijing Enterprises Water Group (BEWG) (Hainan) Co., Ltd for offering the experimental site.

References

[1] F. Yang, Y. Wang, A. Bick, J. Gilron, A. Brenner, L. Gillerman, M. Herzberg, G. Oron, Performance of different configurations of hybrid growth membrane bioreactor (HG-MBR) for treatment of mixed wastewater, Desalination, 284 (2012) 261–268.
[2] T. Leiknes, H. Odegaard, The development of a biofilm membrane bioreactor, Desalination, 202 (2007) 135–143.
[3] X. Huang, K. Xiao, Y. Shen, Recent advances in membrane bioreactor technology for wastewater treatment in China, Front. Environ. Sci. Eng. China, 4 (2010) 245–271.
[4] G. Mannina, G.A. Ekama, M. Capodici, A. Cosenza, D. Di Trapani, H. Odegaard, Moving bed membrane bioreactors for carbon and nutrient removal: the effect of C/N variation, Biochem. Eng. J., 125 (2017) 31–40.
[5] M.J. Palmarin, S. Young, The effects of biocarriers on the mixed liquor characteristics, extracellular polymeric substances, and fouling rates of a hybrid membrane bioreactor, Biochem. Eng. J., 141 (2019) 278–284.
[6] R. Canziani, V. Emondi, M. Garavaglia, F. Malpei, E. Pasinetti, G. Buttiglieri, Effect of oxygen concentration on biological nitrification and microbial kinetics in a cross-flow membrane bioreactor (MBR) and moving-bed biofilm reactor (MBBR) treating old landfill leachate, J. Membr. Sci., 286 (2006)202–212.
[7] H. Prieske, A. Drews, M. Kraume, Prediction of the circulation velocity in a membrane bioreactor, Desalination, 231 (2008) 219–226.
[8] X. Yan, K. Xiao, S. Liang, T. Lei, P. Liang, T. Xue, K. Yu, J. Guan, X. Huang, Hydraulic optimization of membrane bioreactor via baffle modification using computational fluid dynamics, Bioresour. Technol., 175 (2015) 633–637.
[9] I. Yamanoi, K. Kageyama, Evaluation of bubble flow properties between flat sheet membranes in membrane bioreactor, J. Membr. Sci., 360 (2010) 102–108.
[10] R. Liu, X. Huang, Y.F. Sun, Y. Qian, Hydrodynamic effect on sludge accumulation over membrane surfaces in a submerged membrane bioreactor, Process Biochem., 39 (2003) 157–163.
[11] A. Drews, Membrane fouling in membrane bioreactors-characterization, contradictions, cause and cures, J. Membr. Sci., 363 (2010) 1–28.
[12] A. Menniti, E. Morgenroth, The influence of aeration intensity on predation and EPS production in membrane bioreactors, Water Res., 44 (2010) 2541–2553.
[13] Q. Wu, X. Yan, K. Xiao, J. Guan, T. Li, P. Liang, X. Huang, Optimization of membrane unit location in a full-scale membrane bioreactor using computational fluid dynamics, Bioresour. Technol., 249 (2018) 402–409.
[14] J. Gimbun, C.D. Rielly, Z.K. Nagy, Modelling of mass transfer in gas liquid stirred tanks agitated by Rushton turbine and CD-6 impeller: a scale-up study, Chem. Eng. Res. Des., 87 (2009) 437–451.
[15] L. Zhu, D.T. Monteil, Y. Wang, B. Song, D.L. Hacker, M.J. Wurm, X. Li, Z. Wang, F.M. Wurm, Fluid dynamics of flow fields in a disposable 600 mL orbitally shaken bioreactor, Biochem. Eng. J., 129 (2018) 84–95.
[16] E. Amini, M.R. Mehrnia, S.M. Mousavi, N. Mostoufi, Experimental study and computational fluid dynamics simulation of a full-scale membrane bioreactor for municipal wastewater treatment application, Ind. Eng. Chem. Res., 52 (2013) 9930–9939.
[17] X. Yan, Q. Wu, J. Sun, P. Liang, X. Zhang, K. Xiao, X. Huang, Hydrodynamic optimization of membrane bioreactor by horizontal geometry modification using computational fluid dynamics, Bioresour. Technol., 200 (2016) 328–334.
[18] M. Yang, Y. Wei, X. Zheng, F. Wang, X. Yuan, J. Liu, N. Luo, R. Xu, D. Yu, Y. Fan, CFD simulation and optimization of membrane scouring and nitrogen removal for an airlift external circulation membrane bioreactor, Bioresour. Technol., 219 (2016) 566–575.
[19] N. Ratkovich, T.R. Bentzen, Comparison of four types of membrane bioreactor systems in terms of shear stress over the membrane surface using computational fluid dynamics, Water Sci. Technol., 68 (2013) 2534–2544.
[20] F. Rezvani, H. Azargoshasb, O. Jamialahmadi, S. Hashemi-Najafabadi, S. Mohammad, M. Seyed, A. Shojaosadati, Experimental study and CFD simulation of phenol removal by immobilization of soybean seed coat in a packed-bed bioreactor, Biochem. Eng. J., 101 (2015) 32–43.
[21] J. Adanez, A. Abad, F. Garcia-Labiano, P. Gayan, L. de Diego, Progress in chemical looping combustion and reforming technologies, Prog. Energy Combust. Sci., 38 (2012) 215–282.
[22] S. Wang, H. Lu, F. Zhao, G. Liu, CFD studies of dual circulating fluidized bed reactors for chemical looping combustion processes, Chem. Eng. J., 236 (2014) 121–130.
[23] M. Seo, T.D.B. Nguyen, Y. Lim, S. Kim, S. Park, B.H. Song, Y.J. Kim, Solid circulation and loop-seal characteristics of a dual circulating fluidized bed: experiments and CFD simulation, Chem. Eng. J., 2 (2011) 803–811.
[24] T.D.B. Nguyen, M. Seo, Y. Lim, B. Song, S. Kim, CFD simulation with experiments in a dual circulating fluidized bed gasifier, Comput. Chem. Eng., 36 (2012) 48–56.
[25] Y. Yin, Y. Wang, Application of computational fluid dynamics (CFD) in chemical engineering, Petrochem. Technol., 7 (2000) 166–169.
[26] B. Wu, Advances in the use of CFD to characterize, design and optimize bioenergy systems, Comput. Electron. Agric., 93 (2013) 195–208.
[27] S. Schneiderbauer, A. Aigner, S. Pirker, A comprehensive frictional-kinetic model for gas–particle flows: analysis of fluidized and moving bed regimes, Chem. Eng. Sci., 80 (2012) 279–292.
[28] A.B. Harichandan, T. Shamim, CFD analysis of bubble hydrodynamics in a fuel reactor for a hydrogen-fueled chemical looping combustion system, Energy Convers. Manage., 86 (2014) 1010–1022.
[29] Y. Wang, Performance Simulation of Boiling Heat Transfer of R417A Inside Horizontal Smooth and Internally Grooved Tubes, Xi'an University of Science and Technology, 2010.
[30] X. Chen, Simulation Analysis of Establishing a Drainage System Based on FLUENT, Tianjin University, 2012.
[31] C. Xia, Simulation and Analysis of Drainage System Based on FLUENT [D], Tianjin University, 2012.
[32] S.J. Gelderbloom, D. Gidaspow, R.W. Lyczkowski, CFD simulations of bubbling/collapsing fluidized beds for three geldart groups, AlChE J., 49 (2003) 844–858.
[33] M. Bayat, M.R. Mehrnia, N. Mostoufi, M.R. Hamaneh, Investigating wastewater treatment in MBRs using computational fluid dynamics, J. Environ. Stud., 41 (2015) 1–3.
[34] M. Ji, G. Dong, J. Huo, Numerical simulation for hydraulic characteristics in moving bed biofilm reactor, China Water Wastewater, 18 (2002)14–17.
[35] Y. Wu, X. Du, K. Song, H. Liu, J. Wang, E. Wang, Numerical simulation analysis of flow characteristics of suspended packing in biological contact oxidation tank, J. Chem. Ind. Eng., 7 (2018) 3242–3248.
[36] C. Loha, H. Chattopadhyay, P.K. Chatterjee, Assessment of drag models in simulating bubbling fluidized bed hydrodynamics, Chem. Eng. Sci., 75 (2012) 400–407.
[37] P. Pei, K. Zhang, D. Wen, Comparative analysis of CFD models for jetting fluidized beds: the effect of inter-phase drag force, Powder Technol., 221 (2012) 114–122.
[38] J. Zhang, H. Sun, Z. Zhou, A research on the features of new suspending media of moving bed biofilm process, J. Saf. Environ., 2 (2002) 42–44.

[39] F. Yang, A. Bick, S. Shandalov, A. Brenner, G. Oron, Yield stress and rheological characteristics of activated sludge in an airlift membrane bioreactor, J. Membr. Sci., 334 (2009) 83–90.
[40] S. Li, W. Cheng, M. Wang, C. Chen, The flow patterns of bubble plume in an MBBR, J. Hydrodyn. Ser. B, 23 (2011) 510–515.
[41] D. Gu, Z. Liu, Z. Xie, L. Jun, C. Tao, Y. Wang, Numerical simulation of solid-liquid suspension in a stirred tank with a dual punched rigid-flexible impeller, Adv. Powder Technol., 28 (2017) 2723–2734.
[42] S. Xiong, C. Li, Application of MBBR in micro-polluted raw water pretreatment, Water Wastewater Eng., 36 (2010) 25–29.